Journal of Natural Gas Science and Engineering 68 (2019) 102893

Contents lists available at ScienceDirect

Journal of Natural Gas Science and Engineering

journal homepage: www.elsevier.com/locate/jngse

A strain based approach to calculate disparities in pore structure between shale basins during permeability evolution

B. Schwartz[a,*], K. Huffman[b], D. Thornton[c], D. Elsworth[a]

[a] G3 Center, The Pennsylvania State University, University Park, USA
[b] Chevron Mid-continent Business Unit, Midland, USA
[c] Chevron Energy Technology Company, Houston, USA

ARTICLE INFO

Keywords:
Shale permeability
Marcellus shale
Wolfcamp shale
Pore
Geometry
Mineral distribution

ABSTRACT

We test the permeability response of Marcellus shale and Wolfcamp shale under changing strain. While magnitude of strain for a given stress is determined predominantly through mineral composition, the response of transport properties to a given strain are dependent on pore density, pore geometry, and rock fabric/mineral distribution around pores. We characterize the differences between the two shales using bulk mineralogy, SEM imaging with elemental analysis, and the cubic law for permeability evolution. We find that the Marcellus shale is comprised predominantly of clays that leads to more deformation when stressed than the Wolfcamp shale which is composed predominantly of quartz and calcite. The level of creep and compaction are directly related to the amount of clay in each shale sample. A novel result of our study is a strain-driven model to capture permeability evolution in shale due to differences in pore structure.

1. Introduction

Permeabilities within shale reservoirs represent different length scales (Curtis, 2002). First order permeability of a stimulated rock volume involves 1. fractures induced by hydraulic stimulation which create a highly conductive pathway that increases the overall permeability of the reservoir and 2. preexisting natural fractures which are the result of subsurface processes that occur during burial, organic maturation, and the application of tectonic stress (Engelder, 1985; Hancock & Engelder, 1989; Engelder et al., 2009). While the permeability of these features are orders of magnitude higher than that of the matrix permeability, it is critical to point out that permeability decreases through time in these features during depletion due to creep and proppant embedment. The surface area of these features is thought to impact initial production.

Second order permeability in shales is found in the solid matrix between fractures. Within the rock matrix, there exist small pathways between grain boundaries that allow for hydrocarbon storage, localized migration, and migration to larger fractures and adjacent porous reservoirs. While the permeability of these features is orders of magnitude less than that of the induced and stimulated fracture system, they still play a critical role in the ultimate recovery of the well. There are two sets of such flow paths which create distinct, orthogonal permeabilities: one plane oriented in the bedding-parallel direction and one in the bedding-perpendicular direction. The flow paths in the bedding-perpendicular direction are often typified as highly tortuous nano-sized capillary tubes (Javadpour et al., 2007; Javadpour, 2009; Civan et al., 2012), whereas the flow paths in the bedding-parallel direction can be modelled as long penny-shaped slit-like cracks (Li and Elsworth, 2014; Kumar et al., 2015). Many studies have focused on characterizing the flow in the bedding-perpendicular direction: the purpose of this study is to better understand the flow in the bedding-parallel direction, as this is critically important for understanding long-term well performance.

Within the matrix, shale is an orthotropic material with a dominant fracture set in the bedding-parallel direction (Crook, 2002; Bonnelye, 2017). The dominant fracture set is composed of long, penny-shaped fractures separated by finely laminated bedding planes (Bandyodaphyay, 2009) of the order of 1–100 μm in separation (Ulm and Abousleiman, 2006; Horne, 2013). The fracture apertures in the bedding-parallel direction are thought to range between 0.01 and 0.5 microns—a range which allows for diffusion-driven flow as the aperture approaches the mean free path of the gas molecules (Javadpour, 2009; Civan, 2013). This fracture set is responsible for the majority of flow at this scale; permeability in the bedding-parallel direction has been found to be 10 to 100 times higher than permeability in the bedding-perpendicular direction (Bolton et al., 2000; Kwon et al., 2004; Pan et al., 2015).

Many investigators have focused on characterizing the nano-tube

* Corresponding author. 110 Hosler Building, University Park, 16802, USA.
E-mail address: schwartz@psu.edu (B. Schwartz).

https://doi.org/10.1016/j.jngse.2019.05.006
Received 5 March 2019; Received in revised form 21 May 2019; Accepted 21 May 2019
Available online 24 May 2019
1875-5100/ © 2019 Elsevier B.V. All rights reserved.

driven flow in the bedding-perpendicular direction and have found that the no-slip boundary condition used to develop laminar flow models is no longer valid at fracture diameters in the 1 nm–50 nm range (Javadpour, 2009; Civan et al., 2012). Measured permeabilities in shales range from 10^{-23} m^2 to 10^{-17} m^2 (Daigle, 2017). Darcy driven flow dominates from approximately 10^{-20} m^2 to 10^{-17} m^2, whereas molecular diffusion and Knudsen flow must be accounted for when permeability reaches approximately 10^{-21} m^2 or lower (Brown et al., 1946; Civan et al., 2012). These ranges are not absolute, and an understanding of the fracture set geometry and distribution within the matrix remain critical parameters for characterizing permeability and flow through these tight rocks.

Permeability is a dynamic metric: drilling (Islam et al., 2009), fracing (Daigle, 2017), creep (Sinha et al., 2013), and seismic events (Polak et al., 2003; Candela et al., 2014) have all been shown to alter the initial permeability. A change in permeability is caused by either a change in flow channel diameter or fracture coalescence (Eberhardt et al., 1999). In both cases, deformation is the main contributor to changes in the fracture geometry. At stresses that are well below the ultimate strength of the rock matrix, compressive deformation initially closes fractures, whereas fractures begin to coalesce as compressive stress approaches the ultimate strength (Walsh, 1966; Scholz, 1968).

There are three key parameters that define a fracture set geometry within a shale: the fracture length *a*, the fracture aperture *b*, and the fracture spacing *s*. The aspect ratio α of a capillary tube is the ratio b/a and ranges from unity for circular tubes to a limit of zero for long cracks. The ability to flow fluid through a fracture set is predominantly a function of the fracture aperture, and gas production is typically modelled as flow between parallel plates (Goodman, 1989). Of equal importance is the fracture spacing—if the fractures are dense then permeability will be higher, whereas permeability will be lower where the spacing between fractures is large. Fracture spacing is known to be related to bedding thickness (Ladeira, 1981; Narr, 1991) and the degree of rock compaction during burial (Chang et al., 2009). Spacing is often proportional to fracture aperture (Garrett and Bailey, 1977). While it will vary spatially, the spacing, determined by permeability measurements, will reflect an average (Narr, 1996; Ortega et al., 2006). In joint sets, the spacing between fractures is known to remain constant after a certain compressive strain threshold (Wu and Pollard, 1995).

Elsworth (1989) explored permeability evolution in fractured media when the change in aperture was due to deformation of the solid bedding planes and was controlled by *s*. This assumption is valid when mineral stiffness is much larger than fracture stiffness or when *s* is much larger than *b*. In the case of shale matrix, there currently exists no quantitative link between the bedding planes—which are finely laminated mineral ensembles—and fracture spacing. The aim of this work is to quantify the spacing and apertures in shales, the spacing-to-aperture ratio, and to allow the determination of these two variables.

In addition to differences in pore geometry and fracture density, shales also exhibit a range of mineralogical composition which influences material properties. The bulk modulus and shear modulus of a rock can be approximated if its mineralogical composition is known, as these values will be an average of individual elastic moduli of each mineral (Voigt, 1889; Reuss, 1929; Hill, 1952; Clark, 1966; Simmons and Wang, 1971). Shale is a class of rocks typified by low permeability and high clay content. However, the variation in mineralogy between shale basins is large, resulting in widely variable bulk responses to changes in stress (Sone and Zoback, 2013). The main mineral constituents of shale, besides clays and organic material—quartz, feldspars, carbonates, and pyrite—have rigid grains and resist mechanical compaction to a greater degree than clays (Gu and Mildner, 2016). Variations in mineralogy lead to variations in the distribution of bulk elastic and non-elastic deformation.

A common feature of shales that makes them difficult to characterize in the laboratory is time-dependent compaction. After a shale sample has been reintroduced to stress, it will continue to compact for a period ranging from hours to weeks (Sinha et al., 2013). The magnitude of this compaction is variable, and the permeability reduction experienced during this time can be either negligible or several orders of magnitude. A critical unknown in the laboratory is whether this time dependent compaction is a feature that reservoir rocks will experience during drilling and completion operations and pressure depletion or whether it is simply the rock returning to its *in situ* configuration after being exhumed and fully stress-relieved. As this compaction is noted in both outcrop and cored samples, it is believed to be a condition that can be activated during drilling and completions activities. As mineralogy is heterogenous throughout a reservoir, the mechanical response to reactivated compaction is complex. An understanding of pore structure throughout the reservoir is required to understand the response of transport properties to reactivated compaction.

For shales that have high proportions of organic matter, the porosity is mainly within the organic matter itself (Loucks et al., 2009). Much of the remainder of the porosity is in the clay—predominantly illite and smectite (Sondergeld et al., 2010; Curtis et al., 2012). This leads to a potential mismatch in deformation modulus between the minerals surrounding the pore space and the minerals within the matrix. Regardless of overall mineralogy, dissolution of silica or calcite over geologic timescales can lead to cementation of pore boundaries (Berger et al., 1997; Metz et al., 2005). Published values of elastic moduli for various minerals suggest that this disparity of mineral distribution around pores can cause a mismatch in material properties that could span several orders of magnitude (Mavko & Mukerji, 1998; Mavko et al., 2009).

In addition to fracture spacing and mineral distribution, pore geometries of shales are known to differ between basins. Aspect ratios vary from 0.05 to almost 1.0 in Permian Basin shales, whereas the Bakken shale has an average aspect ratio of 0.10 (Bandyopadhyay, 2009; Sone and Zoback, 2013). The additional aperture closure that results from decreasing aspect ratios at the same strain may contribute substantially to permeability evolution where two shales are characterized by different aspect ratios. In this study, we further explore the mineralogical differences between the Marcellus shale and Wolfcamp shale. We use the cubic law to solve for fracture spacing and aspect ratio for these two basins. We incorporate differences in mineral distribution around pores into our strain-driven model and find that permeability evolution with evolving strains can be described with these variables.

2. Characterization techniques

We perform a suite of experiments on cylindrical samples of Marcellus and Wolfcamp shale loaded into a triaxial vessel. Samples are stressed and allowed to compact until no additional deformation is measured by an LVDT placed on the outside of the triaxial vessel. Compaction lasts anywhere from a few hours to a few days. We measure permeability evolution with evolving strains and different pore fluids using pressure pulse tests. Mineralogic data are collected on samples before loading them into the triaxial vessel.

2.1. SEM imaging

In addition to experimental data, we gather SEM images from our samples. We perform elemental analysis on two separate samples for the Marcellus shale and two for the Wolfcamp shale (Fig. 1). We include elemental analyses for calcium, aluminum, and silicon as proxies for calcite, clays, and quartz—we note that silicon will be present in clays as well as in quartz grains. Fig. 1 shows a greater concentration of silicon where quartz is located, whereas measurements in clays do not generally show such high concentrations. As can be seen in Fig. 1, the Marcellus sample shows much higher clay composition with calcite and quartz embedded in a clay matrix, whereas the Wolfcamp samples show much higher quartz and calcite composition. The scale of the Marcellus samples are both approximately 250 μm per edge, whereas the scale of

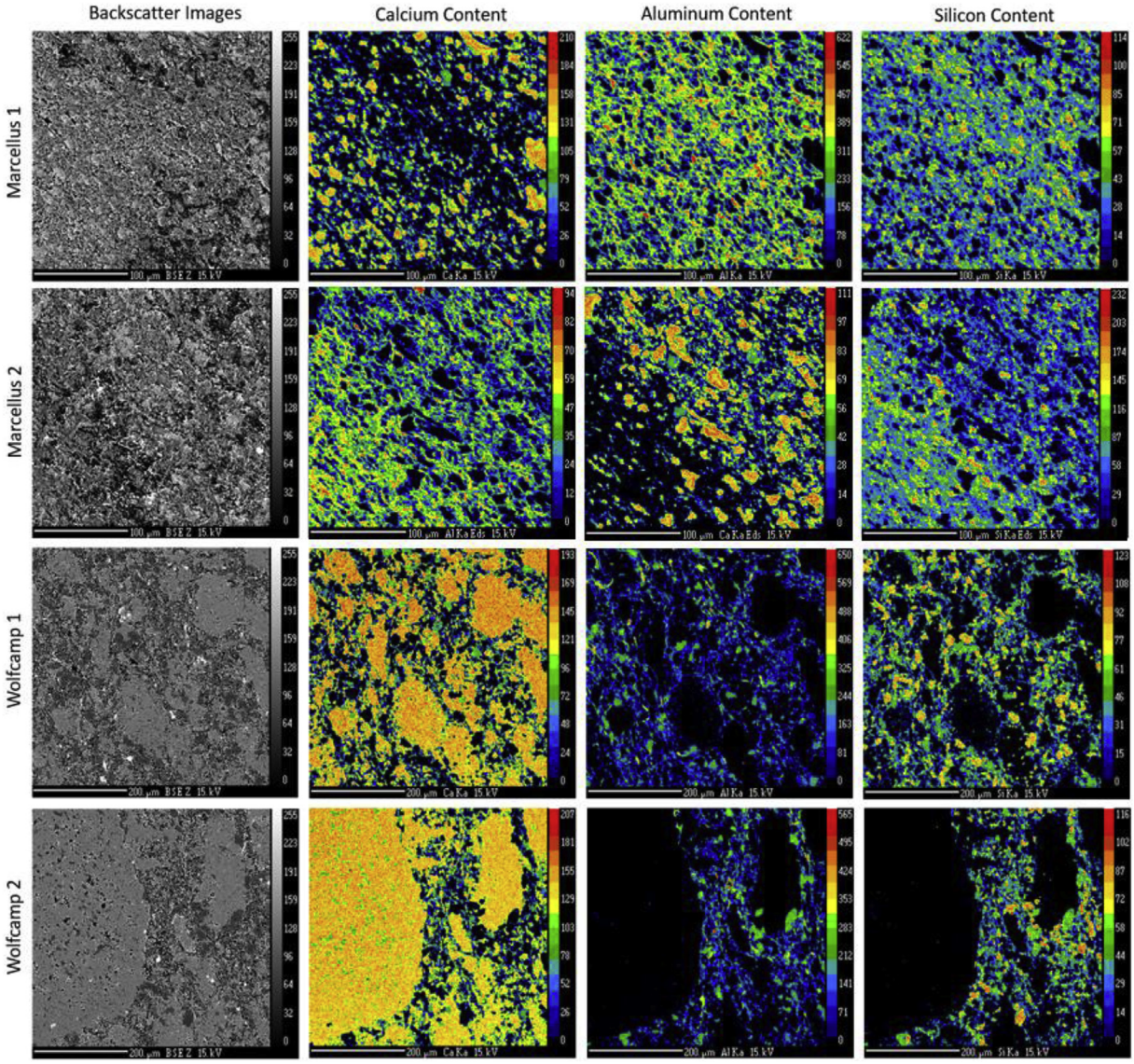

Fig. 1. SEM images of Marcellus and Wolfcamp shales. Each row shows (from left to right) a backscatter image, calcium content, aluminum content, and silicon content as proxies for calcite, clays, and quartz.

the Wolfcamp samples are approximately 500 μm per edge. Thus, the Wolfcamp images display four times more area due to the size of individual grains being large compared to the Marcellus. Because the Marcellus grains are much smaller, the images are cropped twice as close per edge to ensure meaningful resolution.

The images of Fig. 1 are typical for the samples investigated. As can be seen in the column of backscatter images, the fabric of these two shales are categorically different. This is confirmed in the second column, where the calcium content of the Wolfcamp sample is much higher than that in the Marcellus sample. While these are both shales, the differences in depositional environment, burial history, thermal maturation, and mineral migration are apparent as the clay content of the Marcellus samples appears to be quite high compared to that of the Wolfcamp samples.

In order to capture the effect of mineral distribution on permeability evolution, we denote the stiffness of minerals that constitute pore boundaries with K_{sk} and the stiffness of minerals distributed in the matrix further away from pores with K_m. In this parlance, K_{sk} is chosen to describe the stiffness of the "skeletal" minerals filling a pore—the grains that keep the pore open against stress applied normal to the pore boundary. K_{sk} and K_m do not refer to specific minerals, but rather the stiffness of those minerals. K_{sk}/K_m values greater than unity would likely be indicative of pores surrounded by quartz or calcite with clays and organics being found further away from pores. A much more common scenario for shales would be K_{sk}/K_m less than unity, which would indicate that pores are found within clays and organics whereas stiffer minerals such as calcite and quartz would be distributed further away in the surrounding matrix. A K_{sk}/K_m value of unity would indicate that the stiffness of minerals along pore boundaries is identical to the stiffness of minerals in the surrounding matrix. When a compressive deformation is applied, the distribution of that deformation will depend on K_{sk}/K_m. Two rocks could experience the same bulk deformation, but the rock with a lower K_{sk}/K_m will have a larger loss of permeability due to the deformation being concentrated in the softer minerals that make up the pore boundary. These images suggest that in the Marcellus K_{sk}/K_m may be less than unity—pores are surrounded by softer clays and organic matter that concentrates local deformation around the pores themselves.

2.2. Mineralogic data

A third-party vendor conducted X-Ray Powder Diffraction (XRD)

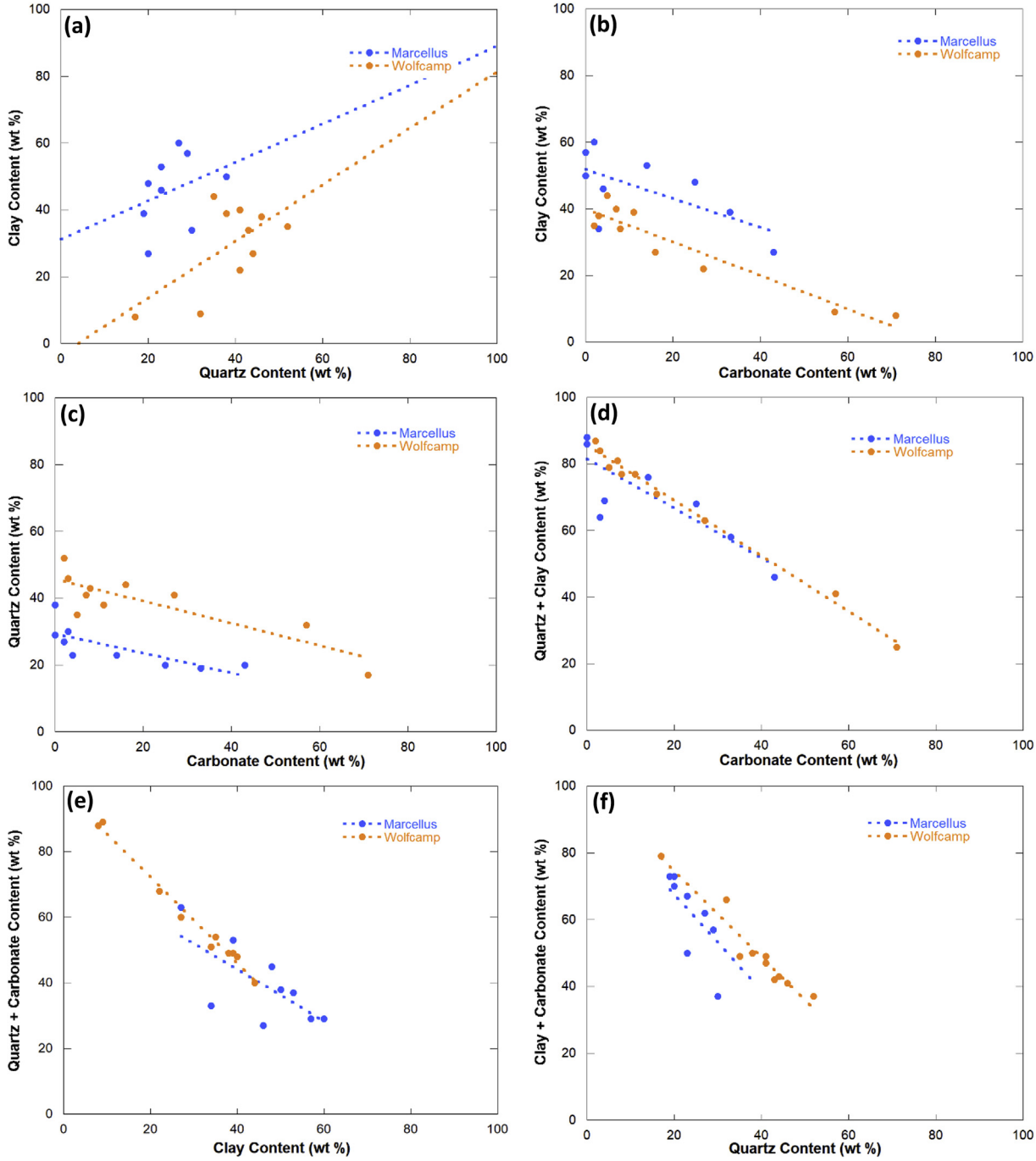

Fig. 2. Cross plots of mineralogy by weight % for Wolfcamp samples and Marcellus samples. Fig. 2a displays clay content vs. quartz content and shows that the Marcellus typically has higher clay composition. Fig. 2b displays clay content vs. carbonate content. Fig. 2c displays quartz content vs. carbonate content and shows that the Wolfcamp samples have higher quartz composition. Fig. 2d shows quartz + clay vs. carbonate content. All values for both basins fall along a straight line. Fig. 2e displays quartz + carbonate vs. clay and shows that the Wolfcamp is predominantly quartz and carbonates whereas the Marcellus is predominantly clay. This suggests a mismatch in mineral distribution around pores. Fig. 2f displays clay + carbonate content vs. quartz content.

spectroscopy to determine mineralogy for both the Marcellus and Wolfcamp samples. We find that, in general, the Marcellus samples are clay-rich with lesser amounts of quartz or carbonates than the Wolfcamp samples. In Fig. 2 the clay content of Marcellus samples are generally higher than in the Wolfcamp samples, whereas the Wolfcamp has larger amounts of quartz and carbonates. These three minerals account for most of the composition for each sample, although organic matter (1–4%), pyrite (< 2%), and other minerals are found to lesser degrees. Fig. 2a shows that values for clay content in the Marcellus range from 27% to 60% by weight and in the Wolfcamp range from 8% to 44% by weight. Quartz values range from 19% to 38% in the Marcellus and in the Wolfcamp from 17% to 52% by weight. Fig. 2b shows clay content cross-plotted with carbonate content. In both basins, as carbonate content increases, clay content decreases. The carbonate content in the Marcellus ranges from 0% to 43% and in the Wolfcamp from 2% to 71%. Fig. 2d shows the combined quartz content and clay content compared to the carbonate content with results for both basins showing an identical linear trend. Fig. 2e and f shows cross-plots for different combinations of quartz, clay, and carbonates.

For the Wolfcamp shale samples we gather acoustic data and density

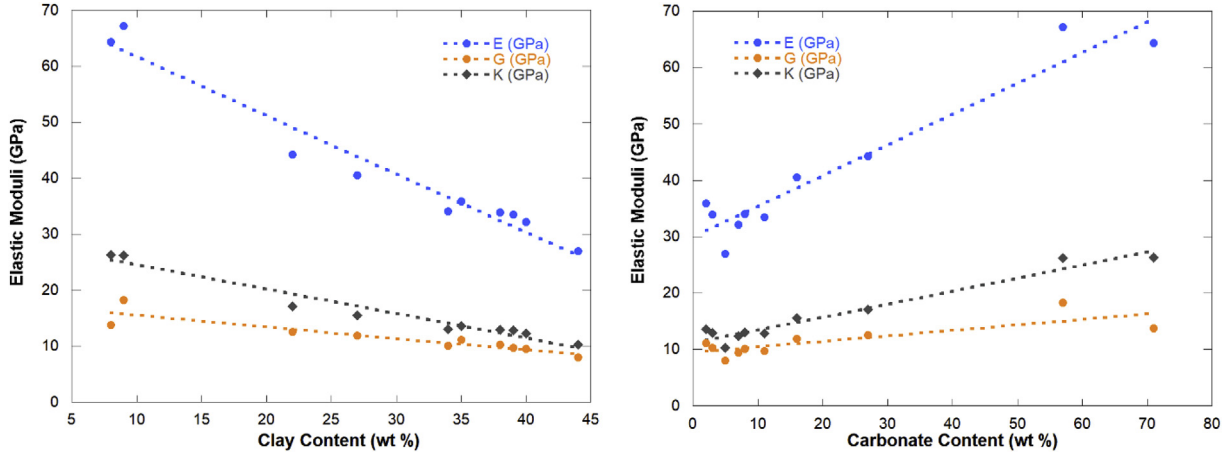

Fig. 3. Elastic moduli of Wolfcamp samples with varying mineralogy. E, G, and K all decrease with increasing clay content (LHS) and decreasing carbonate content (RHS).

data. We use the standard equations to convert V_p, V_s, ν and ρ into K, G, and E:

$$K = \rho\left(V_p^2 - \frac{4}{3}V_s^2\right) \quad (1)$$

where K is the bulk modulus, ρ is the rock density, and V_p and V_s are the compressional and shear wave velocities, respectively.

$$G = \rho V_s^2 \quad (2)$$

where G is the shear modulus.

$$E = 2\rho V_S^2(1 + \nu) \quad (3)$$

where E is the Young's modulus and ν is the Poisson ratio.

$$\nu = \frac{V_p^2 - 2V_s^2}{2(V_p^2 - V_s^2)} \quad (4)$$

We then plot elastic moduli against mineralogy. V_p ranged from 3.5 to 5.6 km/s and V_s ranged from 2.1 to 3.2 km/s. Density ranged from 1450 to 1835 kg/m^3. Poisson ratio ranged from 0.18 to 0.28 with most values falling between 0.19 and 0.22.

In Fig. 3 we see that all three of the moduli decrease with increasing clay content and increase with increasing carbonate content. Because the mineral stiffness of quartz is intermediate between calcite and clays, the relationship between quartz content and deformation modulus is neutral when compared to the other two and is not included in Fig. 3. Values for bulk modulus K ranges from 10 GPa to 26 GPa as the clay content ranges from 8% to 44% and carbonate content ranged from 2% to 71%. Bulk modulus for clay ranges from 1.5 GPa for Kaolinite to 25 GPa for Gulf clays, whereas quartz is 37 GPa, calcite is 64–77 GPa, and kerogen is 2.9 GPa (Mavko et al., 2009). These values suggest that the minerals found in the Wolfcamp must be on the low end of the ranges provided by Mavko et al. (2009).

2.3. Time dependent compaction data

We compile compaction data from six Marcellus shale samples. All samples are loaded to 24 MPa hydrostatic stress and allowed to compact until there was no additional deformation. Deformation is measured at a rate of 1 Hz. Fig. 4 shows compaction over approximately 8 h. In this case, positive strain is compressive. These curves are compared to mineralogic data and it is found that the magnitude of compaction is directly related to the clay composition of each sample. The right axis of Fig. 4 shows the clay content of each sample and provides an excellent match.

Time dependent compaction is a common problem for shale in the laboratory (Sinha et al., 2013). During our experimental suite we measure permeability evolution with pore pressure using helium and methane in series. As can be seen in Fig. 5, the Marcellus sample does not exhibit the expected behavior. The helium curve should be monotonically increasing, as the only elastic effect should be poromechanical expansion. However, as time dependent compaction is also occurring, both the helium and methane curves are rotated downward. On the right-hand side of Fig. 5 is a set of curves for the Wolfcamp shale. There is not the same time dependent compaction visible in the Wolfcamp sample, as can be seen by permeability enhancement with increasing pore pressure for helium. Looking closer at the mineralogy of these two samples, both have an organic content of 3%, resulting in similar wedges between the helium curve and the methane curve due to adsorptive permeability loss with methane. However, the Marcellus sample is 50% clay whereas the Wolfcamp sample is only 38% clay. Later we show that the creep driven permeability loss is also due to the additional pore compressibility within the Marcellus.

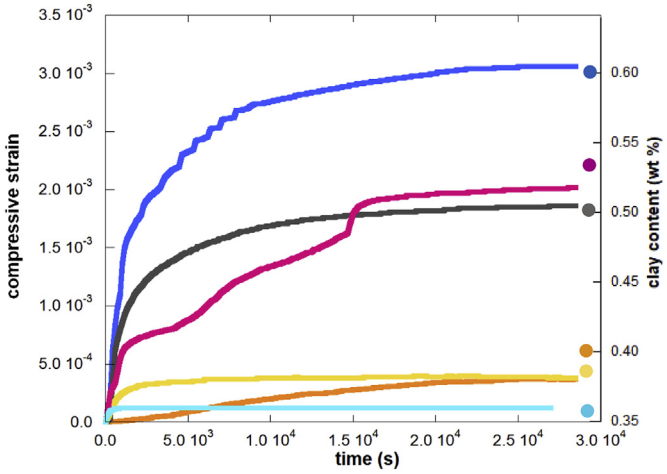

Fig. 4. Compaction after loading (left) is related to % clay content (right).

2.3.1. Permeability evolution with strains

Following samples compaction, permeability evolution was measured under varied strain. In general, Marcellus samples experienced a much larger reduction of permeability compared to the Wolfcamp samples. In Fig. 6 we plot permeability evolution versus strain for a representative run from each shale basin. The permeability evolution in the Wolfcamp was quite different than in the Marcellus. As can be seen in Fig. 6, the Marcellus sample experienced a 100-fold permeability

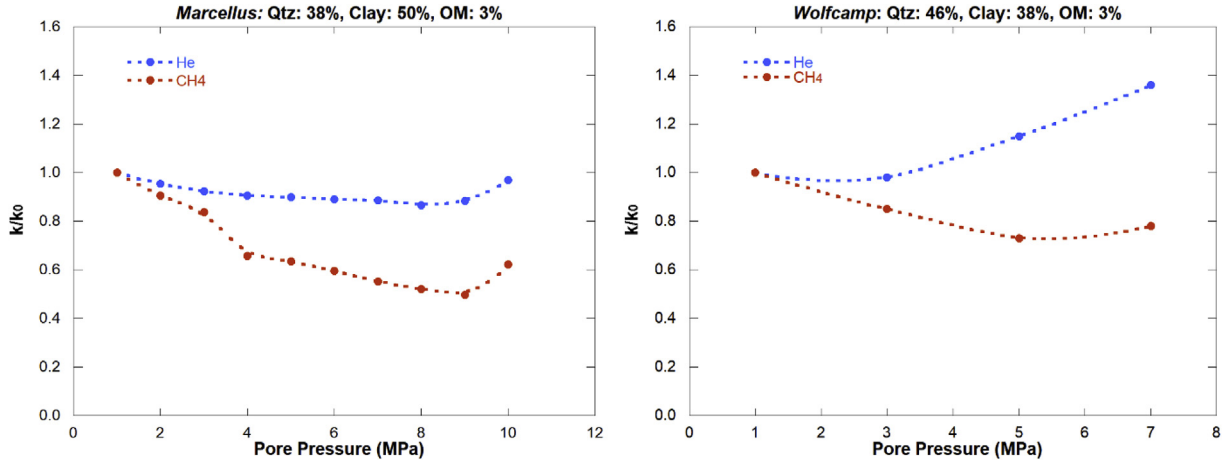

Fig. 5. Permeability evolution vs. pore pressure. The blue curve representing helium should be monotonically increasing due to poromechanical expansion, as is seen on the RHS for the Wolfcamp sample. The downward shift of the curves on the LHS is due to time dependent compaction throughout the experiment. Both shale samples are 3% organic matter, which is seen in the adsorptive permeability loss between the helium and methane curves for each sample.

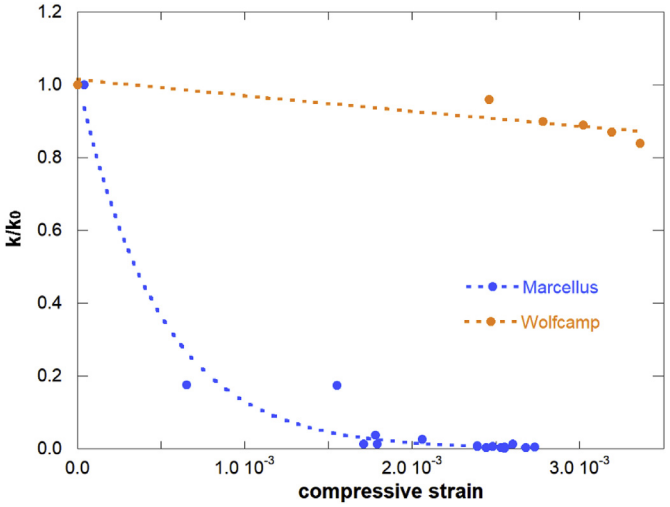

Fig. 6. The same magnitude of strain in Marcellus samples produce very large permeability loss compared to the same level of strain in Wolfcamp samples.

reduction compared to the Wolfcamp at the same amount of external strain.

An LVDT measures the mean axial strain of a sample, and whether the localized departure of strain from the mean is important depends on several factors. In the case of mean strain measured alongside permeability of a shale sample saturated with a single fluid, there are several considerations to be evaluated. A bulk permeability measurement reflects the mean pore channel aperture within the sample (Narr, 1996) such that using mean strain in a permeability model is appropriate. However, one scenario in which the strain will be distributed unevenly is when a sample is composed of minerals with very different individual deformation moduli. In that instance, strain would be concentrated in the softer components. If the permeable pathways are also concentrated in the softer components—such as the flow conduits in the Marcellus being concentrated in clays and organic matter—then the permeability loss for a given compressive mean strain will be larger than for a sample in which permeable pathways are not concentrated in the softer components. Therefore, a departure from the mean strain due to mineral distribution around pores must be considered in any permeability model for materials with mineral constituents of varying deformation moduli.

3. Characterization using the cubic law

The cubic law can be modified to explore the roles of fracture spacing, fracture geometry, and mineral distribution around pores. First, we derive an expression for the spacing to aperture ratio s/b in terms of permeability evolution with strain. Then, we modify that expression to solve for average aspect ratio b/a. We can use the mineralogical constraints to reconcile the differences in permeability evolution with the mineral distribution around the pore space as captured by K_{sk}/K_m.

3.1. Fracture spacing

Next, we examine the disparity between the Wolfcamp and Marcellus shale's permeability evolution by exploring the spacing to aperture ratio s/b. In Fig. 7, the cubic law is used to plot several permeability curves at different spacing to aperture ratios along with the experimental data to illustrate the influence of this variable. As can be seen, the data suggest that the Marcellus shale fracture spacing is much further apart than the Wolfcamp. For fractures that are far apart, the spacing can be the primary driver of permeability evolution.

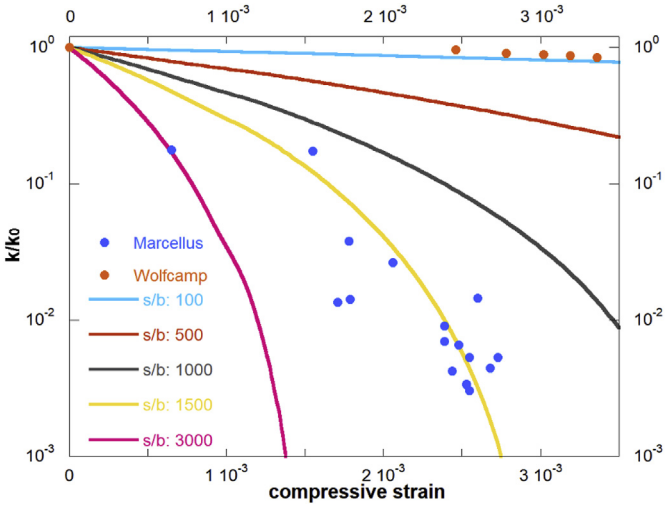

Fig. 7. As s/b increases, permeability is reduced at the same strain. The Marcellus shale permeability data fits an s/b of approximately 1500, whereas the Wolfcamp sample fits an s/b of 50. In this figure, no other influences are considered.

For flow between parallel plates, permeability evolution can be cast as

$$\frac{k}{k_0} = \left(1 + \frac{\Delta b}{b_0}\right)^3 \tag{5}$$

where k is the permeability in m^2, k_0 is the initial permeability, b_0 is the initial aperture, and Δb is the change in aperture—in the case of aperture reduction Δb is negative. In our experiments, we measure deformation along the bedding-parallel fracture set such that the dynamic Poisson ratio is required to convert to deformation perpendicular to the fracture set. To calculate the portion of permeability evolution due to spacing, Δb can be defined as

$$\Delta b = \nu \varepsilon s \tag{6}$$

where ν is the Poisson ratio, ε is the longitudinal strain, and s is the fracture spacing in meters. This changes Eq. (5) to

$$\frac{k}{k_0} = \left(1 - \nu\varepsilon\frac{s}{b_0}\right)^3 \tag{7}$$

Eq. (7) is similar to assuming that the fractures are soft compared to the matrix (Elsworth, 1989):

$$\Delta k = \frac{1}{12s}(b + s\Delta\varepsilon)^3 \tag{8}$$

Because spacing is assumed to be constant, we note that the initial spacing-to-aperture ratio s/b_0 is constant:

$$\frac{s}{b_0} = constant \tag{9}$$

We can therefore rearrange Eq. (7) in terms of this constant ratio:

$$\frac{s}{b_0} = \frac{1}{\nu\varepsilon}\left(1 - \left(\frac{k}{k_0}\right)^{\frac{1}{3}}\right) \tag{10}$$

In the above formulation, the value of the spacing-to-aperture ratio is a constant and represents the role of the fracture spacing in permeability evolution in the absence of other influences. We plot the values of Eq. (10) below in Fig. 8 for a Marcellus sample and a Wolfcamp sample.

3.2. Pore geometry

Exploring the role of pore geometry where α is b/a—pore aperture over pore length—we cast pore compressibility as

$$C_{pc} = \frac{1-\nu}{G}\left(\alpha + \frac{1}{\alpha}\right) \tag{11}$$

The strain in the pore space is related to the effective stress and the pore compressibility:

$$\varepsilon_{pc} = \sigma' C_{pc} \tag{12}$$

The change in aperture Δb/b can be calculated two ways. The first is to assume that the aspect ratio is constant. In that case, the isolated role of pore geometry in determing permeability evolution is

$$\frac{k}{k_0} = (1 - \sigma' C_{pc})^{\frac{3}{2}} \tag{13}$$

As α approaches zero, pore compressibility can be simplified as

$$C_{pc} = \frac{1-\nu}{G\alpha} \tag{14}$$

such that

$$\varepsilon_{pc} = \varepsilon\frac{1-\nu}{\alpha} \tag{15}$$

where we differentiate between the pore strain ε_{pc} and the bulk external strain ε. Setting Eq. (7) and Eq. (13) equal to each other:

$$\left(1 - \varepsilon\frac{1-\nu}{\alpha}\right)^{\frac{1}{2}} = 1 - \nu\frac{s}{b_0}\varepsilon \tag{16}$$

Expanding the right hand side creates a 2nd order polynomial

$$1 - \varepsilon\frac{1-\nu}{\alpha} = 1 - 2\nu\frac{s}{b_0}\varepsilon + \nu^2\frac{s^2}{b_0^2}\varepsilon^2 \tag{17}$$

Which simplifies to

$$\frac{a}{b}(1-\nu) = \nu\frac{s}{b_0}\left(2 - \nu\frac{s}{b_0}\varepsilon\right) \tag{18}$$

Noting that b/b_0 is $k/k_0^{1/3}$ this expression becomes

$$\frac{a}{s} = \frac{\nu}{1-\nu}\left(\frac{k}{k_0}\right)^{\frac{1}{3}}\left(1 + \left(\frac{k}{k_0}\right)^{\frac{1}{3}}\right) \tag{19}$$

Eq. (15) is valid when the aspect ratio α is assumed constant. This need not be the case, and in the event that α changes due to fracture closure then Eq. (13) becomes

$$\frac{k}{k_0} = (1 - \sigma' C_{pc})^3 \tag{20}$$

This term a/s may be isolated by equating Eq. (7) and Eq. (20) to yield

$$1 - \varepsilon\frac{1-\nu}{\alpha} = 1 - \nu\frac{s}{b_0}\varepsilon \tag{21}$$

This simplifies to

$$\frac{a}{b}(1-\nu) = \nu\frac{s}{b_0} \tag{22}$$

Such that

$$\frac{a}{s} = \frac{\nu}{1-\nu}\left(\frac{k}{k_0}\right)^{\frac{1}{3}},\ variable\ \alpha \tag{23}$$

The results from Eq. (19) and Eq. (23) are applied to the data for the Marcellus and Wolfcamp samples and are plotted below in Fig. 9.

The solutions we are interested in are for the case of variable α. The value of a/s for the Marcellus is approximately 0.20 and for the Wolfcamp is approximately 0.40. This is a valuable constraint, because later it will allow us to define the aspect ratio in terms of the spacing. With Eq. (10) and Eq. (23), the initial aspect ratio α_0 can be calculated.

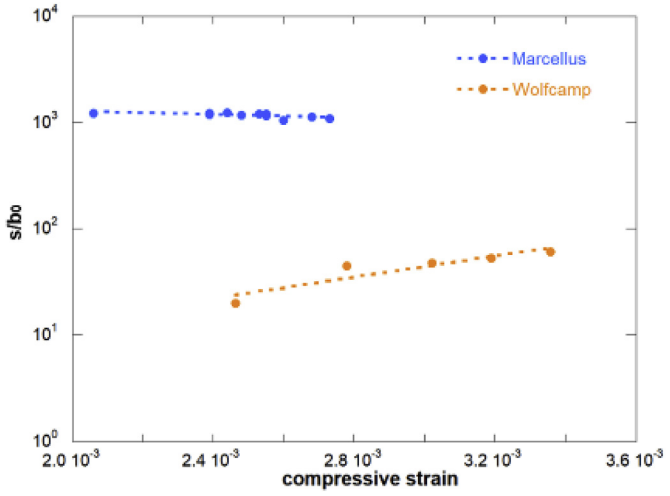

Fig. 8. Calculated fracture spacing using permeability and strain data in Equation (10) with a Poisson ratio of 0.22. In the absence of other influences, the Marcellus has a high spacing over 10^3 whereas the Wolfcamp is approximately 50.

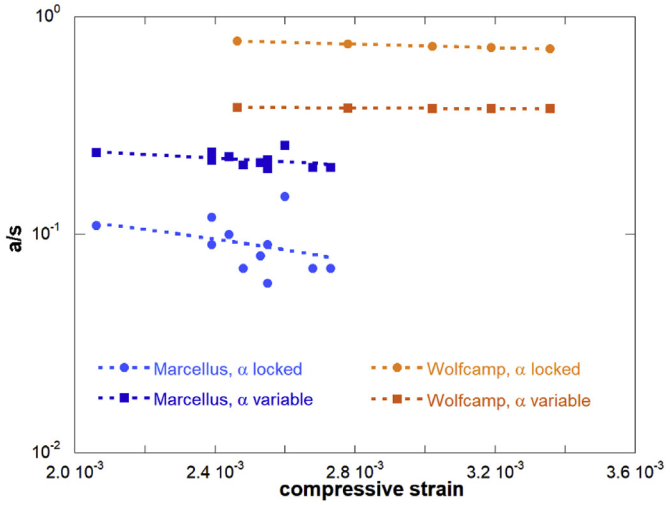

Fig. 9. Fracture length to spacing a/s. Both Eq. (19) and Eq. (23) are shown.

As strain was parallel to the ellipsoid major semi-axis, changes in aspect ratio are primarily from changes in aperture Δb. Any Δa can be assumed neglible for the experiment's configuration, such that b_0/a should provide a good estimate of α_0. Combining Eq. (10) and Eq. (23) give

$$\frac{b_0}{a} = \frac{\frac{b_0}{s}}{\frac{a}{s}} = \frac{\varepsilon(1-\nu)}{\left(\frac{k}{k_0}\right)^{\frac{1}{3}}\left(\left(\frac{k}{k_0}\right)^{\frac{1}{3}}-1\right)} \tag{24}$$

The results of equation (24) are plotted for each sample below in Fig. 10. We can see in Fig. 10 that the aspect ratio for the Wolfcamp is approximately five times larger than in the Marcellus. In the absence of other influences, the Marcellus α is approximately 10^{-2}, and the Wolfcamp is approximately 5×10^{-2}. Eq. (20) suggests that this alone can result in a 50% difference in permeability evolution.

3.3. Mineral distribution around the pore space

In order to capture the effect of mineral distribution around pores, we created a simple pore model using COMSOL Multiphysics in which the stiffness of the minerals directly surrounding an elliptical pore was varied relative to the matrix stiffness K_m. This "pore skeleton" stiffness K_{sk} was varied between 10^{-3} to 10^{3} of K_m in order to create the

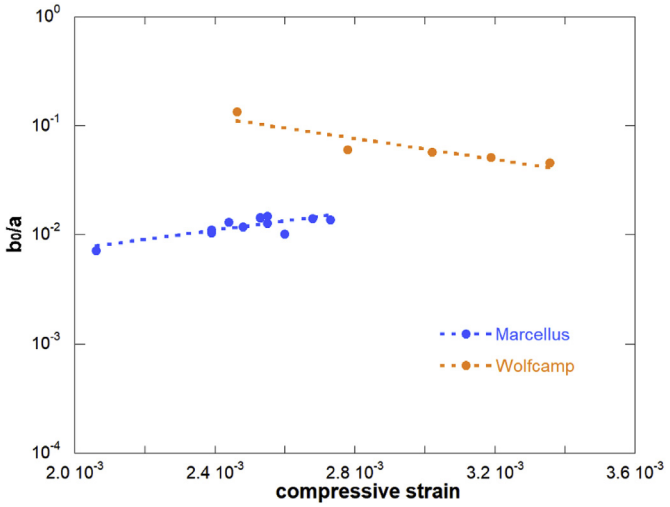

Fig. 10. Calculated initial aspect ratio for both the Marcellus and Wolfcamp samples.

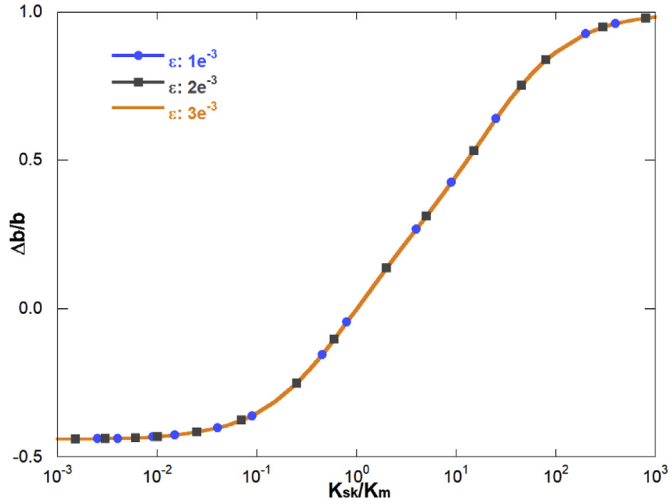

Fig. 11. Changing aperture with varying pore mineral stiffness. Results are normalized to K_{sk}/K_m equal to 1, and show that if a grain mismatch creates a pore mineral stiffness less than the surrounding matrix stiffness, additional aperture is lost. The results are independent of strain.

dimensional ratio K_{sk}/K_m. We measured the change in aperture Δb/b at different strains and plot the results below in Fig. 11. When values are normalized to K_{sk}/K_m equal to 1, we note that the solution becomes independent of strain. This is useful, as it reduces the number of variables that are dependent on strain by one. Fig. 11 should be interpreted as the additional change in aperture as a result of pore mineral stiffness. Values below this threshold represent softer minerals allowing for greater pore closure due to strain. Values above this threshold correct the aperture loss associated with other influences when the minerals around pores are stiffer than the surrounding matrix.

3.4. Integrating all variables

In the above sections, fracture spacing s/b, pore geometry α, and mineral stiffness K_{sk}/K_m were analyzed as independent variables in order to understand their individual contributions to permeability evolution. Now they are analyzed in conjunction with each other to provide a more complete characterization of the pore structure of shales. The complete equation for permeability evolution is

$$\frac{k}{k_0} = \left(1 + \left(\frac{\Delta b}{b_0}\right)_{\frac{s}{b}} + \left(\frac{\Delta b}{b_0}\right)_{\alpha} + \left(\frac{\Delta b}{b}\right)_{\frac{K_{sk}}{K_m}}\right)^3 \tag{25}$$

where the influence of fracture spacing s/b, pore geometry α, and mineral stiffness K_{sk}/K_m are defined based on the change in pore aperture that they are each responsible for. The last term for K_{sk}/K_m does not have an analytical solution, but we can use Fig. 11. Mineral stiffness varies within one order of magnitude. It is expected that most mismatches will be close to K_{sk}/K_m equal to unity; however, the variance in aperture around this value is large. Having developed equations for the other terms, we can recast equation (25) as

$$\frac{k}{k_0} = \left(1 + \nu\varepsilon\frac{s}{b_0} + \varepsilon\frac{1-\nu}{\alpha} + \left(\frac{\Delta b}{b}\right)_{\frac{K_{sk}}{K_m}}\right)^3 \tag{26}$$

Recalling from Fig. 9 that a/s is approximately 0.2 for the Marcellus and 0.4 for the Wolfcamp, we can constrain the relationship between s/b_0 and α:

$$\frac{a}{s} = c \rightarrow \frac{a}{b_0} = c\frac{s}{b_0} \tag{27}$$

such that Eq. (26) becomes

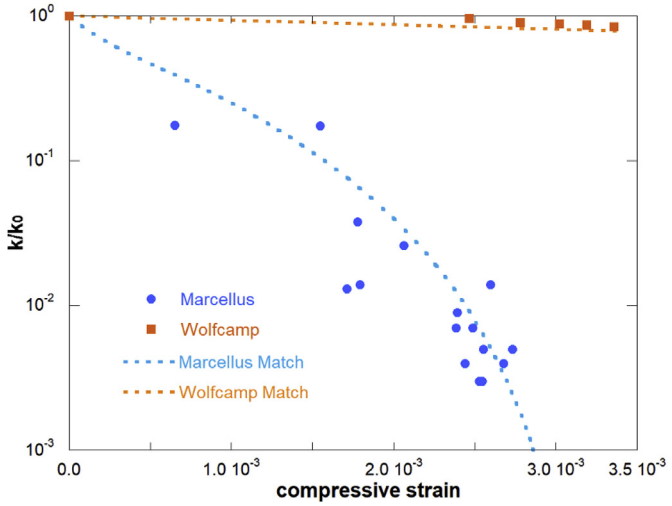

Fig. 12. Experimental data for permeability and strain plotted with Eq. (28) for the Marcellus and Wolfcamp basins. The values used to match the Marcellus data were s/b_0 equal to 700, α equal to $7e^{-3}$, and K_{sk}/K_m equal to 0.7. The values used to match the Wolfcamp data were s/b_0 equal to 40, α equal to $6e^{-2}$, and K_{sk}/K_m equal to 1.0.

$$\frac{k}{k_0} = \left(1 - \varepsilon\left(\nu\frac{s}{b_0} + c\frac{s}{b_0}(1-\nu)\right) + \left(\frac{\Delta b}{b}\right)_{\frac{K_{sk}}{K_m}}\right)^3 \tag{28}$$

The value of c in Eq. (28) is 0.2 for the Marcellus and 0.4 for the Wolfcamp. Having eliminated α, we can use a best fit for s/b_0 and the change in aperture due to mineral stiffness from Fig. 11. We find that the values that best fit the permeability and strain data are s/b equal to 700 for the Marcellus and 40 for the Wolfcamp, α equal to 0.007 for the Marcellus and 0.06 for the Wolfcamp, and K_{sk}/K_m of 0.7 for the Marcellus and 1.0 for the Wolfcamp. This suggests that the Wolfcamp has a much higher fracture density than the Marcellus, allowing for strain to be distributed among more fractures. It also shows that the aspect ratio of the Marcellus pores make them more compressible than in the Wolfcamp. Casting the Marcellus as softer pores in a stiff matrix than the Wolfcamp recovered the remaining variance between Eq. (28) and the experimental data. The matches to the pemeability versus strain curves are below in Fig. 12.

4. Conclusion

We show that the Marcellus shale is predominantly clay while the Wolfcamp shale is predominantly quartz and calcite. This disparity in mineralogy is the basis for the differences in mechanical response to stress, including time dependent compaction upon initial loading. The magnitude of creep-induced strain is related to the clay content. Compaction reduces permeability in the lab and may reduce it in field operations as well. At constant stress, shale compaction is a function of mineralogy. At constant strain, permeability evolution is a function of pore stiffness and pore density. Pore stiffness is determined by pore geometry and distribution of minerals around the pore space. As fracture spacing increases, fracture compliance also increases as strain becomes distributed among fewer fractures.

Shales will experience different levels of permeability evolution at the same level of strain depending on their mineralogy, mineral distribution around flow channels, flow channel geometry, and fracture density. All of these observations point to a complex response within a heterogenous shale reservoir with the introduction of a new stress or strain. We show that the Marcellus shale is characterized by high clay content as well as high fracture spacing, slit-like pores, and soft pores in a stiffer matrix. The Wolfcamp shale is characterized by high quartz and calcite content, lower fracture spacing, and rounder pores. These differences highlight that shales require additional characterization and understanding the differences in pore structure is critical to predicting permeability evolution from evolving stress. There are several pore characterization methods that could be used to concurrently validate this strain-driven model, and we recommend additional studies incorporating such techniques to refine this model as necessary for field-specific considerations.

Acknowledgements

This work is a partial result of support from Chevron Energy Technology Company, and their support is gratefully acknowledged. We also thank three anonymous reviewers, whose recommendations have helped improve this manuscript.

Appendix A. Supplementary data

Supplementary data to this article can be found online at https://doi.org/10.1016/j.jngse.2019.05.006.

References

Bandyopadhyay, K., 2009. Seismic Anisotropy: Geological Causes and its Implications to Reservoir Geophysics. Stanford University.
Berger, G., Lacharpagne, J.C., Velde, B., Beaufort, D., Lanson, B., 1997. Kinetic constraints on illitization reactions and the effects of organic diagenesis in sandstone/shale sequences. Appl. Geochem. 12 (1), 23–35.
Bolton, A.J., Maltman, A.J., Fisher, Q., 2000. Anisotropic permeability and bimodal pore-size distributions of fine-grained marine sediments. Mar. Pet. Geol. 17 (6), 657–672.
Bonnelye, A., Schubnel, A., David, C., Henry, P., Guglielmi, Y., Gout, C., et al., 2017. Elastic wave velocity evolution of shales deformed under uppermost crustal conditions. J. Geophys. Res.: Solid Earth 122 (1), 130–141.
Brown, G.P., DiNardo, A., Cheng, G.K., Sherwood, T.K., 1946. The flow of gases in pipes at low pressures. J. Appl. Phys. 17 (10), 802–813.
Candela, T., Brodsky, E.E., Marone, C., Elsworth, D., 2014. Laboratory evidence for particle mobilization as a mechanism for permeability enhancement via dynamic stressing. Earth Planet. Sci. Lett. 392, 279–291.
Chang, C.P., Angelier, J., Huang, C.Y., 2009. Subduction Zone Geodynamics.
Civan, F., Rai, C.S., Sondergeld, C.H., 2012. Determining shale permeability to gas by simultaneous analysis of various pressure tests. SPE J. 17 (03), 717–726.
Civan, F., 2013. Comparison of control volume analysis and porous media averaging for formulation of porous media transport. In: Modelling and Simulation in Fluid Dynamics in Porous Media. Springer, New York, NY, pp. 27–53.
Clark, S.P. (Ed.), 1966. Handbook of Physical Constants, vol. 97 Geological Society of America.
Crook, A.J., Yu, J.G., Willson, S.M., 2002. January). Development of an orthotropic 3D elastoplastic material model for shale. In: SPE/ISRM Rock Mechanics Conference. Society of Petroleum Engineers.
Curtis, M.E., Sondergeld, C.H., Ambrose, R.J., Rai, C.S., 2012. Microstructural investigation of gas shales in two and three dimensions using nanometer-scale resolution imaging Microstructure of Gas Shales. AAPG Bull. 96 (4), 665–677.
Curtis, J.B., 2002. Fractured shale-gas systems. AAPG Bulletin 86 (11), 1921–1938.
Daigle, H., Hayman, N.W., Kelly, E.D., Milliken, K.L., Jiang, H., 2017. Fracture capture of organic pores in shales. Geophys. Res. Lett. 44 (5), 2167–2176.
Eberhardt, E., Stead, D., Stimpson, B., 1999. Quantifying progressive pre-peak brittle fracture damage in rock during uniaxial compression. Int. J. Rock Mech. Min. Sci. 36 (3), 361–380.
Elsworth, D., 1989, July. Thermal permeability enhancement of blocky rocks: one-dimensional flows. Int. J. Rock Mech. Min. Sci. Geomech. Abstr. 26 (3–4), 329–339 (Pergamon).
Engelder, T., 1985. Loading paths to joint propagation during a tectonic cycle: an example from the Appalachian Plateau, USA. Journal of Structural Geology 7 (3-4), 459–476.
Engelder, T., Lash, G.G., Uzcátegui, R.S., 2009. Joint sets that enhance production from Middle and Upper Devonian gas shales of the Appalachian Basin. AAPG Bulletin 93 (7), 857–889.
Garrett, K.W., Bailey, J.E., 1977. Multiple transverse fracture in 90 cross-ply laminates of a glass fibre-reinforced polyester. J. Mater. Sci. 12 (1), 157–168.
Goodman, R.E., 1989. Introduction to Rock Mechanics, vol. 2 Wiley, New York.
Gu, X., Mildner, D.F.R., 2016. Ultra-small-angle neutron scattering with azimuthal asymmetry. J. Appl. Crystallogr. 49 (3), 934–943.
Hancock, P.L., Engelder, T., 1989. Neotectonic joints. Geological Society of America Bulletin 101 (10), 1197–1208.
Hill, R., 1952. The elastic behaviour of a crystalline aggregate. Proc. Phys. Soc. 65 (5), 349.
Horne, S.A., 2013. A statistical review of mudrock elastic anisotropy. Geophys. Prospect. 61 (4), 817–826.
Islam, M., Skalle, P., Faruk, A.M.M., Pierre, B., 2009, January. Analytical and numerical study of consolidation effect on time delayed borehole stability during underbalanced

drilling in shale. In: Kuwait International Petroleum Conference and Exhibition. Society of Petroleum Engineers.
Javadpour, F., Fisher, D., Unsworth, M., 2007. Nanoscale gas flow in shale gas sediments. J. Can. Pet. Technol. 46 (10).
Javadpour, F., 2009. Nanopores and apparent permeability of gas flow in mudrocks (shales and siltstone). J. Can. Pet. Technol. 48 (08), 16–21.
Kumar, H., Elsworth, D., Mathews, J.P., Marone, C., 2016. Permeability evolution in sorbing media: analogies between organic-rich shale and coal. Geofluids 16 (1), 43–55.
Kwon, O., Kronenberg, A.K., Gangi, A.F., Johnson, B., Herbert, B.E., 2004. Permeability of illite-bearing shale: 1. Anisotropy and effects of clay content and loading. J. Geophys. Res.: Solid Earth 109 (B10).
Ladeira, F.L., Price, N.J., 1981. Relationship between fracture spacing and bed thickness. J. Struct. Geol. 3 (2), 179–183.
Li, X., Elsworth, D., 2015. Geomechanics of CO2 enhanced shale gas recovery. J. Nat. Gas Sci. Eng. 26, 1607–1619.
Loucks, R.G., Reed, R.M., Ruppel, S.C., Jarvie, D.M., 2009. Morphology, genesis, and distribution of nanometer-scale pores in siliceous mudstones of the Mississippian Barnett Shale. J. Sediment. Res. 79 (12), 848–861.
Mavko, G., Mukerji, T., 1998. Bounds on low-frequency seismic velocities in partially saturated rocks. Geophysics 63 (3), 918–924.
Mavko, G., Mukerji, T., Dvorkin, J., 2009. The Rock Physics Handbook: Tools for Seismic Analysis of Porous Media. Cambridge University Press.
Metz, V., Amram, K., Ganor, J., 2005. Stoichiometry of smectite dissolution reaction. Geochem. Cosmochim. Acta 69 (7), 1755–1772.
Narr, W., Suppe, J., 1991. Joint spacing in sedimentary rocks. J. Struct. Geol. 13 (9), 1037–1048.
Narr, W., 1996. Estimating average fracture spacing in subsurface rock. AAPG Bull. 80 (10), 1565–1585.
Ortega, O.J., Marrett, R.A., Laubach, S.E., 2006. A scale-independent approach to fracture intensity and average spacing measurement. AAPG Bull. 90 (2), 193–208.
Pan, Z., Ma, Y., Connell, L.D., Down, D.I., Camilleri, M., 2015. Measuring anisotropic permeability using a cubic shale sample in a triaxial cell. J. Nat. Gas Sci. Eng. 26, 336–344.
Polak, A., Elsworth, D., Yasuhara, H., Grader, A.S., Halleck, P.M., 2003. Permeability reduction of a natural fracture under net dissolution by hydrothermal fluids. Geophys. Res. Lett. 30 (20).
Reuss, A., 1929. A. Reuss, Z. Angew. Math. Mech. 9. pp. 49 (1929). Z. Angew. Math. Mech., 9, 49.
Scholz, C.H., 1968. Experimental study of the fracturing process in brittle rock. J. Geophys. Res. 73 (4), 1447–1454.
Simmons, G., Wang, H., 1971. A Handbook of Single Crystal Elastic Constants and Calculated Aggregate Properties.
Sinha, S., Braun, E.M., Determan, M.D., Passey, Q.R., Leonardi, S.A., Boros, J.A., et al., 2013. March). Steady-state permeability measurements on intact shale samples at reservoir conditions-effect of stress, temperature, pressure, and type of gas. In: SPE Middle East Oil and Gas Show and Conference. Society of Petroleum Engineers.
Sondergeld, C.H., Newsham, K.E., Comisky, J.T., Rice, M.C., Rai, C.S., 2010. January). Petrophysical considerations in evaluating and producing shale gas resources. In: SPE Unconventional Gas Conference. Society of Petroleum Engineers.
Sone, H., Zoback, M.D., 2013. Mechanical properties of shale-gas reservoir rocks—Part 1: static and dynamic elastic properties and anisotropy. Geophysics 78 (5), D381–D392.
Ulm, F.J., Abousleiman, Y., 2006. The nanogranular nature of shale. Acta Geotechnica 1 (2), 77–88.
Voigt, W., 1889. On the relation between the elasticity constants of isotropic bodies. Ann. Phys. Chem 274, 573–587.
Walsh, J.B., 1966. Seismic wave attenuation in rock due to friction. J. Geophys. Res. 71 (10), 2591–2599.
Wu, H., Pollard, D.D., 1995. An experimental study of the relationship between joint spacing and layer thickness. J. Struct. Geol. 17 (6), 887–905.